10-2019

Dynamic Response Modeling of High-Speed Planing Craft with Enforced Acceleration

Gene Hou

Brain Johnson

Jonathan Degroff

Steven Trenor

Jennifer Michaeli

Ocean Engineering 192 (2019) 106493

Contents lists available at ScienceDirect

Ocean Engineering

journal homepage: www.elsevier.com/locate/oceaneng

Dynamic response modeling of high-speed planing craft with enforced acceleration

Gene Hou [a,*], Brian Johnson [a], Jonathan Degroff [a], Steven Trenor [a], Jennifer Michaeli [b]

[a] Department of Mechanical and Aerospace Engineering, Old Dominion University, Norfolk, VA, 23454, USA
[b] Department of Engineering Technology, Old Dominion University, Norfolk, VA, 23454, USA

ARTICLE INFO

Keywords:
Finite element model
ND NASTRAN
PATRAN
Planing hulls
Enforced acceleration
Rigid inflatable boat (RIB)
Sea trials
Wave impact
Base excitation

ABSTRACT

An approach is investigated in this study for structural dynamic analysis of a high-speed planing hull, in which the pointwise acceleration data collected from sea trials are enforced as base excitation. The paper first performed the full boat analysis of an 11-meter high speed craft for a period of one wave impact selected from each of nine seakeeping runs. The sea trial acceleration data collected from 11 accelerometers placed close to the centerline and the keel are enforced as input, while those from 3 accelerometers placed around the pilot cabin are selected for validation. The substructure dynamic analysis of the isolated pilot cabin was then conducted and validated, in which 7 pointwise enforced accelerations are selected from the simulation output of the full boat dynamic analysis. The substructure dynamic analysis enables detailed investigation of local stress concentrations where critical equipment and personnel are located. The proposed approach can be extended to rigid-flexible body coupling analysis of a high-speed craft when it is running with large pitching and yawing motion.

1. Introduction

Small fast vessels are usually equipped with planing hulls to increase speed. The planing hull will locally generate high hydrodynamic pressure in high speed to reduce friction drag and wave resistance. Unfortunately, a planing hull craft often encounters high slamming loads with high encountering frequency. Such slamming can suddenly alter sailing direction and speed, and creates hazardous conditions, not only for those individuals aboard but also for the traversing sea vessel itself, from boat hull to onboard equipment. In order to mitigate risk, it is important that steps are taken to ensure the sea vessel is structurally sound for safe operation.

The slamming phenomena of a planing hull involves fully coupled dynamic interaction between fluid, structure, wind, wave and the vessel itself. It is a very challenging undertaking to fully understand the slamming phenomena and its consequences on the design and operation of a planing hull. It has drawn attention of many researchers in the past. To aid these efforts, many drop-wedge tests, towing tank tests, sea trials and numerical simulations have been conducted to collect the data on pointwise accelerations, pressures and strains on planing hulls. Based upon the collected data, Allen et al. (1978) introduced a semi-empirical equation that correlates the impact pressure to the value of the 1/10th highest peak vertical acceleration. Similar semi-empirical equations to estimate the impact pressure in terms of different levels of average acceleration have been developed and incorporated in design and safety rules, chosen by various classification societies such as American Bureau of Shipping (ABS), Det Norske Veritas (DNV), or Lloyd's Register (Grimsley et al., 2010). The different levels of the averaged vertical acceleration required in these impact pressure equations can be approximated in terms of wave height, forward speed and geometry features of the planing hull (Savitsky and Brown, 1976; Hoggard and Jones, 1980). As an example, Ojeda and his colleagues (2004) employed this approach to conduct a finite element analysis of a composite catamaran under static slamming load. In their study, both the impact pressure and the averaged acceleration are estimated based upon the DNV rules and assumed to be uniformly distributed through the wetted areas. The different levels of averaged acceleration may also be directly represented in terms of the statistical parameters of the experimentally collected acceleration data. In this case, the collected acceleration data is commonly assumed to follow an exponential distribution, as suggested early by Fridsma (1971).

Recent studies have cautioned the use of the Allen and Jones' equation. These new investigations have come about by conducting new experiments or by numerical simulation. Riley et al. (2010, 2016) have

* Corresponding author.
E-mail address: ghou@odu.edu (G. Hou).

https://doi.org/10.1016/j.oceaneng.2019.106493
Received 11 March 2019; Received in revised form 10 August 2019; Accepted 22 September 2019
Available online 29 October 2019

pointed out the need of standardizing the definition of a slamming event to better characterize acceleration data. Razola et al. (2014) improved the accuracy of the Allen and Jones' equation by modifying the existing load-carrying area aspect ratio and adding a new factor to count for the load transverse reduction. Furthermore, some researchers have questioned the use of the exponential distribution to quantify the peak acceleration data (Razola et al., 2016; VanDerwerken and Judge, 2017). Others have called for a dynamic structural analysis of a planing hull in a slamming event. Dessi and Ciappi (2013) addressed the importance of taking both the impact force and its induced vibration into consideration to identify a slamming event on fast ships. Their conclusion was made based upon the slamming statistics collected from their investigation on the impact dynamics of a high-speed ferry model in a towing tank. Razola et al. (2014) indicated that to design a planing hull serving for a long life requires the understanding of local deformation and stresses under extreme slamming pressure. Joo et al. (2017) and Riley and Peterson (2017) pointed out the need of pointwise impulse acceleration profile right under a crew seat or an on-board equipment, which are important for design of a suitable shock isolation mount for crew and operation safety. These additional design considerations of a safe and robust planing hull require, not only the average design pressure, but the detailed structural responses of the boat at various concerned time instances. This calls for a detailed dynamic structural analysis of the flexible boat in a slamming event.

Full simulation of a slam impact event for a planing hull is still under development, though significant advancement has been made recently. The challenges lie on its multidisciplinary nature, which requires intensive modeling and computational efforts. The emerging approach is to develop a unified set of governing differential equations to cover all involved disciplines which are then solved with a unified numerical mesh and algorithm. This approach is called the closely coupled approach (Hou et al., 2012). Yang (2018) studied the breaking water generated by a free fall rigid body due to an impact. He modeled three different domains: air, fluid and rigid body, in the same form of Navier-Stokes equation in which the velocity and the pressure are the unknowns. This method has yet to be extended to planing hulls.

The commonly used approach at this moment is called the loosely coupled approach (Yang and Huang, 2016). At each time instance, the approach uses independently developed disciplinary models to simulate waves, fluid, and vessel structure separately. The disciplinary solutions are then reconciled based upon the common interface conditions, before moving on to the next time step. The main challenges of this approach lie on the difficulties of accurately tracing the location of the moving boundary and transfer boundary velocity and pressure between domains which are modeled and discretized differently.

In many FSI applications, the structure problem is usually solved by the finite element method. The fluid problem on the other hand can be formulated and solved by a variety of methods. In the case where the Navier-Stokes equation was solved with a fixed grid in the fluid domain, overset grids (Sukas et al., 2017) and immersed method (Yang, 2018) were proposed to overcome the issues of mismatched interface meshes. Others formulated and solved the fluid flow by the Arbitrary Lagrangian -Eulerian technique which incorporates the mesh movement in the fluid domain simulation (Aymone, 2004; Nordanger et al., 2016). The isogeometric finite element approach was employed by Nordanger et al. (2016) to generate domain mesh automatically in each discipline and to produce an exact and smooth parameterization of the interface between domains. Furthermore, a linear static structure subjected to boundary displacement was solved to guide the movement of meshes in the fluid domain. The magnitude of the mesh movement in different areas in the fluid domain can be controlled by assigning different values of Young's modulus to the areas of concern. Recently, the Lagrangian-based, smoothed particle hydrodynamics (SPH) method has been developed and applied to solve various multi-physics problems including fluid-structure interaction (Liu and Liu, 2010). The method can model detailed physics and handle large deformation and breaking surfaces. It usually covers the fluid domain with mesh free particles, each of which occupies a compact support. Along the fluid-structure interface, the SPH method requires an efficient algorithm to calculate the distance between the structure boundary and the nearby fluid particles (Siemann and Langrand, 2017; Hu et al., 2014).

Ma and Mahfuz (2012) simulated the heave and pitch of a multi-hull ship model moving forward with a constant speed in a water tank. Its hull panel, girders and web frames are made of sandwich composite panels. The entire structure is discretized with 3,247 nodes and 3,162 shell elements. ANSYS is used for a coupled fluid and structural analysis, incorporated with harmonic surface waves simulated by a 2D potential flow model. Their results demonstrated that it is important to take the elastic deformation into account in the FSI analysis as it affects the fluid pressure distribution around the ship hull. To further study the detailed failure modes in the web-girder interface, the authors first identified the high stress area from the global FSI analysis which was carried out based on a coarse mesh. The local substructure was then constructed around the high stressed area with refined meshes. The quasi-static analysis of the substructure model was then performed, subjected to the boundary force and displacement values obtained in the global FSI analysis. Xie et al. (2018) investigated a water-entry hydro-elastic problem using FLUENT for fluid dynamics simulation, ANSYS for structural analysis and the volume of fluid method for air-water interface. A constrained minimization was constructed to convert the element center pressure output from FLUENT to nodal pressure input to ANSYS. The simulation results were compared satisfactorily with water entrance testing data.

Stern and his colleagues used their comprehensive software, CFDSHIP-IOWA, which models the viscous fluid domain with moving interface boundary between the vessel and the fluid and models the free surface with the level set method. The surface pressure is first collected to derive the motion of the vessel, which in turn alters the fluid domain boundary. Overset gridding is used for data transfer between interfaced domains. This method enables visualization of physics details in fluid-structure interaction (Carrica et al., 2010). Though this method is comprehensive, it is computationally intensive. In their recent work, elastic deformation was considered only for part of the ship hull and solved by ANSYS finite element code (Volpi et al., 2017). The results compared favorably with the testing results in sea trials. Alternatively, fluid-structure interaction in time domain was carried out only for a rigid vessel. The instantaneous surface pressure was then applied to the finite element model of the flexible vessel to find the dynamic responses in a quasi-static state (Volpi et al., 2017; Faltinsen, 2005).

Recently, Fragassa (2019) conducted FSI simulation of a slamming of the boat hull of a rigid inflatable boat (RIB) entering a calm water tank. The model boat is 4.95 m long and 1.75 m wide. The FSI simulation was done with the framework of the LS-Dyna software in which the boat hull was made of composite materials and discretized with 26,000 shell finite elements and the fluid domain was modeled and solved with the SPH method. The results showed that, during water entry of the boat, the maximal stress happened along the keel, while the maximal deformation happened along the starboard and the port sides of the boat. Fragassa et al., (2019) had also extended the LS-Dyna-based tool to simulate the drop test of a composite laminated cylinder which fell into calm water with different impact velocities. In this research effort, the SPH method was applied to model both air and water. The results showed that including the air in the impact model improved the solution accuracy in predicting the maximal deformation during impact.

The studies of Rosen, Garme, and their colleagues (Razola et al., 2014; 2016) focused on the long-term motion profile of a planing hull. The approach they used is termed as a single disciplinary approach. They solved only the equation of motion of a rigid planing hull for surging, heaving and pitching subjected to the loads integrated from time dependent sectional pressures. These sectional pressures were evaluated based upon the nonlinear strip theory, which was derived from a potential flow model for vertical impact of a 2D wedge. The advantage of this approach is its computational efficiency, which

enables the research team to conduct numerical simulation for a long period of time to generate enough acceleration data for statistical quantification. In their study, they pointed out the importance of setting the maximal allowable displacement and stress values of each panel for the lifelong design of a planing hull. This is because local structure responses are the results of local extreme pressure applied to the flexible boat hull during slamming, not the results of the averaged design pressure. To address this issue, they (Razola et al., 2014) built a finite element model of a section of a boat hull. Structure dynamic analysis was then conducted for the modeled section subjected to a non-uniform pressure distribution reconstructed from the pressure data collected from 12 pressure transducers. The pressure distribution reconstruction strategy was derived based upon the assumption that a fluid particle moves with the same speed during an impact from the keel to the chine on a section of the planing hull (Rosen and Garme, 2004; Rosen, 2005).

The single disciplinary approach will be employed in this paper as well to investigate structural dynamic response of a planing hull slamming event. However, in this study, instead of pressure transducers, the data collected from accelerometers will be used as enforced excitation to simulate the slamming loads. Enforced excitation referred here is a type of dynamic response induced by the time-dependent boundary conditions prescribed in terms of displacement, velocity, or acceleration. Structural analysis through enforced excitation has been conducted on structures in the air and on the ground alike, most notably in the analysis of space shuttle main engine structures and the induced vibration of structures during earthquakes or on a shaker table. The large mass method is commonly used to enforce a single-degree boundary motion, in which the excitation force is set to be equal to the acceleration multiplied by the mass value (Clough and Penzien, 1975). Davis et al. (2012) used the enforced base excitation method to simulate the drop test response of an onboard equipment using a 6 degree-of-freedom (DOF) motion simulator. Using the motion profile measured by a single base accelerometer mounted on the base of the platform as input, the method is proved successful by validation through frequency and transient responses of the onboard equipment. In a broader view, a structure under enforced excitation can be formulated as a differential-algebra equation (DAE), which can be solved by introducing Lagrange multipliers to impose the prescribed boundary motion. The resultant set of equations can be solved by the elimination method or the penalty method (Chandrupatla and Belegundu, 2012). The elimination method separates the displacements into the boundary set and the relative or the interior set (Cho et al., 2016; Flanigan, 1994; Bampton and Craig, 1968; Blades and Craig, 1997). The equation of motion of the entire structure can then be reformulated into two. One is an ordinary differential equation solved for the interior or the relative displacements while the other is an algebra equation directly used to compute the value of the Lagrange multipliers. The penalty method has been commonly used in finite element problems for static structural analysis or dealing with incompressibility conditions in velocity-pressure flow problems (Reddy, 1984), though seldom used in the time-dependent problems. The work of Liu and Lu (2010) is an example which applied the penalty method to count for earthquake base excitation in seismic analysis of structures. Scovazzi et al. (2017) proposed an interesting approach, which not only achieves accurate velocity as well as stresses but accommodates easily with enforced velocity and stress boundary conditions. Their equation of motion is expressed in terms of the first order time derivatives of stresses and velocities.

The structural dynamic analysis of an 11-meter Zodiac H1110 (2005) Rigid Inflatable Boat (RIB) under a slamming event will be investigated here. This is done by adopting the enforced motion analysis capability provided by the commercially available finite element analysis software, ND PATRAN and NASTRAN, which is built upon the elimination approach (2010) to handle single point acceleration constraints. The report of this investigation is organized and grouped into four sections; Methods and Materials, Full Boat Validation, Accelerometer Placement and Substructure Application. Section 2 covers the methods and materials employed in this study. This section is made of three sub-sections. Section 2.1 briefly outlines the derivation of the equation of motion subjected to pointwise acceleration constraints. This constrained dynamic equation forms the mathematical base for structural dynamic analysis under enforced excitation. The required input variables for solving the derived equation of motion are the finite element data of the 11-meter RIB of concern and the acceleration data collected during the sea trials of the same boat. The details of the former are presented in Section 2.2 and the latter in Section 2.3. Section 3 reports the validation process which is done by taking advantage of the commercially rated NASTRAN software to perform the enforced structural dynamic analysis of the 11-meter RIB. Pointwise acceleration profiles collected from eleven accelerometers during sea trials are filtered and prepared as input for these dynamic analyses. The proposed enforced base excitation method was then validated by comparing the simulated acceleration output with the associated data collected at three above-deck accelerometers from sea trials. Section 4 investigates the effects of the placement and the number of input accelerometers on the accuracy of numerical simulation. It is followed by Section 5 where the dynamic analysis of the pilot cabin is conducted. The pilot cabin is separated from the hull boat as an isolated substructure. The acceleration profiles are enforced at the selected 7 points located at the base of the pilot cabin. Values of these 7 input acceleration profiles are taken from the numerical simulation of the full boat analysis. Section 6 is the final section which concludes this study with conclusion remarks and suggestions for future study.

2. Methods and materials

The first part of this section presents the detailed derivation of the equation of motion associated with base excitation. The equation of motion is derived based upon the framework of constrained dynamics (Haug, 1989, 1992). This theoretical formulation serves as the foundation for dynamic analysis subjected to enforced acceleration. The input data required for solving the derived equation of motion include the stiffness and mass matrices of the structure and the pointwise acceleration data for base excitation. The second part of this section describes the finite element model of the 11-meter RIB (Corbishdale, 2014), which is the application focus of this study. The last part of this section describes the acceleration data extraction process. This is done with the help of a matlab code, Standard G (Murphy and Planchak, 2015). This code takes the acceleration data as input, filters out the high frequency noise caused by vibration and uses a peak identification algorithm to count the number of peaks. The model, algorithm, and data they provided were essential in the dynamic response analysis of the RIB.

2.1. Equation of motion under base excitation

The equation of motion of a free flexible structure under the given loading $\boldsymbol{p}(t)$ can be described as

$$M\ddot{\boldsymbol{x}}(t) + C\dot{\boldsymbol{x}}(t) + K\boldsymbol{x}(t) = \boldsymbol{p}(t) \tag{1}$$

where M, C and K are the mass, damping and stiffness matrices and $\boldsymbol{p}(t)$ and $\boldsymbol{x}(t)$ are the force and the displacement vectors, respectively. The displacement vector $\boldsymbol{x}(t)$ in Eq. (1) is unknown. The above equation maybe simplified as

$$M\ddot{\boldsymbol{x}}(t) = \boldsymbol{f}(t, \boldsymbol{x}, \dot{\boldsymbol{x}}) \equiv \boldsymbol{p}(t) - C\ddot{\boldsymbol{x}}(t) - K\boldsymbol{x}(t)$$

In the case of enforced motion, a given subset of degrees of freedom of the system are subjected to enforced acceleration, which can be viewed as constraints imposed upon the solution of Eq. (1). That is,

$$M\ddot{\boldsymbol{x}}(t) = \boldsymbol{f}(t, \boldsymbol{x}, \dot{\boldsymbol{x}}) \quad \text{subject to} \quad \ddot{\boldsymbol{x}}_B \equiv \boldsymbol{a}(t) \tag{2}$$

where the displacement vector is divided into two parts, prescribed or free, $\boldsymbol{x}^T = (\boldsymbol{x}_I \quad \boldsymbol{x}_B)$, in which $\boldsymbol{x}_I$ denotes the degrees of freedom free of

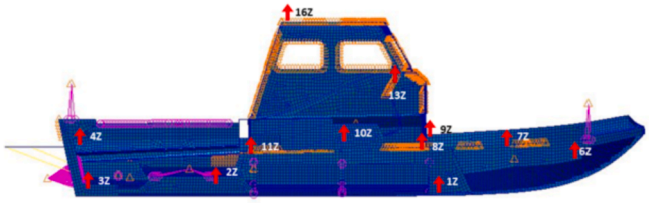

Fig. 1. Side-view of 11-meter cabin RIB model with accelerometer locations.

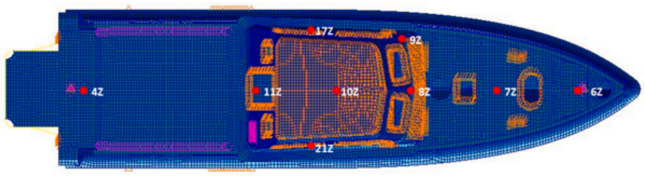

Fig. 2. Top-view of 11-meter cabin RIB model with accelerometer locations.

constraints, while the acceleration associated with $\boldsymbol{x}_B$ are prescribed by the given values, $\boldsymbol{a}(t)$. It should be noted that Eq. (2) can be extended to cases with enforced displacements and velocities (Haug, 1992).

As the constraint is holonomic, Eq. (2), can be augmented by introducing the Lagrange multipliers $\boldsymbol{\lambda}$ as

$$\begin{bmatrix} M_{II} & M_{IB} & 0 \\ M_{BI} & M_{BB} & I \\ 0 & I & 0 \end{bmatrix} \begin{Bmatrix} \ddot{\boldsymbol{x}}_I \\ \ddot{\boldsymbol{x}}_B \\ \boldsymbol{\lambda} \end{Bmatrix} = \begin{Bmatrix} \boldsymbol{f}_I(t, \boldsymbol{x}_I, \dot{\boldsymbol{x}}_I, \boldsymbol{x}_B, \dot{\boldsymbol{x}}_B) \\ \boldsymbol{f}_B(t, \boldsymbol{x}_I, \dot{\boldsymbol{x}}_I, \boldsymbol{x}_B, \dot{\boldsymbol{x}}_B) \\ \boldsymbol{a}(t) \end{Bmatrix} \tag{3}$$

Equation (3) is a DAE index 3 system. The constraint imposed on the system equation is holonomic and with one single degree of freedom,

$$\ddot{\boldsymbol{x}}_B = \boldsymbol{a}(t) \tag{4}$$

which can be directly integrated and result in the velocity and the position constrains, with given initial velocity and position, $\boldsymbol{u}_0$ and $\dot{\boldsymbol{u}}_0$ as

$$\left.\begin{aligned} \dot{\boldsymbol{x}}_B &\equiv \boldsymbol{a}t + \dot{\boldsymbol{u}}_0 \\ x_B &\equiv \frac{1}{2}\boldsymbol{a}t^2 + \dot{\boldsymbol{u}}_0 t + \boldsymbol{u}_0 \end{aligned}\right\} \tag{5}$$

Therefore, the solution of Eq. (3) is not subjected to any hidden constraints on velocity and displacement.

The most convenient way to solve Eq. (3) is by direct substitution of Eq. (4). The resultant equations become

$$\begin{bmatrix} M_{II} & 0 \\ M_{BI} & I \end{bmatrix} \begin{Bmatrix} \ddot{\boldsymbol{x}}_I \\ \boldsymbol{\lambda} \end{Bmatrix} = \begin{Bmatrix} \boldsymbol{f}_I - M_{IB}\boldsymbol{a} \\ \boldsymbol{f}_B - M_{BB}\boldsymbol{a} \end{Bmatrix} \tag{6}$$

The first row of Eq. (6) is a typical ODE which can be solved with help of Eq. (3) as

$$M_{II}\ddot{\boldsymbol{x}}_I = \boldsymbol{f}_I(t, \boldsymbol{x}_I, \dot{\boldsymbol{x}}_I, \boldsymbol{x}_B, \dot{\boldsymbol{x}}_B) - M_{IB}\ddot{\boldsymbol{x}}_B = \boldsymbol{f}_I(t, \boldsymbol{x}_I, \dot{\boldsymbol{x}}_I, \boldsymbol{u}_0, \dot{\boldsymbol{u}}_0, \boldsymbol{a}) - M_{IB}\boldsymbol{a} \tag{7}$$

which yields the solutions, $\boldsymbol{x}_I(t)$ and $\dot{\boldsymbol{x}}_I(t)$. These solutions can be substituted back to the second row of Eq. (6) to compute the Lagrange multiplier as

$$\lambda = \boldsymbol{f}_B(t, \boldsymbol{x}_I, \dot{\boldsymbol{x}}_I, \boldsymbol{x}_B, \dot{\boldsymbol{x}}_B) - M_{BI}\ddot{\boldsymbol{x}}_B = \boldsymbol{f}_B(t, \boldsymbol{x}_I, \dot{\boldsymbol{x}}_I, \boldsymbol{u}_0, \dot{\boldsymbol{u}}_0, \boldsymbol{a}) - M_{BI}\ddot{\boldsymbol{x}}_I - M_{BB}a$$

or more specifically,

$$\boldsymbol{\lambda} = \boldsymbol{f}_B(t, \boldsymbol{x}_I, \dot{\boldsymbol{x}}_I, \boldsymbol{u}_0, \dot{\boldsymbol{u}}_0, \boldsymbol{a}) - M_{BI}M_{II}^{-1}\boldsymbol{f}_I + \left(M_{BI}M_{II}^{-1}M_{IB} - M_{BB}\right)\boldsymbol{a} \tag{8}$$

The Lagrange multiplier represents in fact the constraint force required to enable the system to maintain the prescribed acceleration.

Alternative forms of dynamic equations to express Eq. (2) are available and can be found in the literature for applications in earthquake analysis, launching of space rocket and impact drop test (Cho et al., 2016; Flanigan, 1994; Bampton and Craig, 1968; Blades and Craig, 1997).

2.2. Finite element model of the RIB

The finite element model of a Zodiac H1110 RIB (2005) was originally created by researchers in order to find the approximate ideal locations for the sensors through modal analysis (Corbishdale, 2014). The total length of the boat is 10.82 m with a maximum beam width of 2.68 m. The boat is mainly made of composite and aluminum. Further specifications of the boat can be found on the Zodiac Milpro website listed in the references at the end of this paper. The finite element model of the boat, as shown in Figs. 1 and 2, was originally built by the software FEMAP. The model is made of 50,732 nodes, 211 beam, 50,634 quadrilateral and 798 triangular elements. A total of 45 rigid bars were used to connect key structural nodes on the boat to 4,372 lumped masses. These lumped masses represented the motor (aft), fuel tanks (inside the boat and aft), facility mounts (aft and forward), and other onboard equipment. The rigid bar elements are shown in the model, Figs. 1 and 2, as purple lines and circles. Some of the other nodes in the images of the model are an orange color to represent nodes connected to smeared masses such as armor plating, hatches, windows, radar, and other equipment. The finite element model was later imported to ND NASTRAN and PATRAN which is the finite element code used in this study.

The longitudinal center of gravity (LCG) of the physical boat, as measured from the transom-keel intersection, was approximately 3.18 m with an uncertainty of approximately ±0.872%. The finite element model of the boat had its LCG located at approximately 3.43 m as measured from the transom-keel intersection (Corbishdale, 2014). This difference between the LCG locations on the physical boat and the finite element model is approximately 7.76% which is outside the uncertainty in the LCG measurement of the real-world boat. However, the finite element model of the boat was given the same weight, 15,320 lbs. as its real-world counterpart (Corbishdale, 2014). It is also important to note that both the calm-water and rough-water trials were conducted with a weight of 15,845 lbs. with the addition of crew, seats, ballast and instrumentation; it had reduced fuel, and the rack and bench were removed (Corbishdale, 2014). This also changed the LCG of the physical boat from 3.18 m to 3.22 m from the transom-keel intersection (Corbishdale, 2014).

The modal analysis of the RIB boat was initially conducted by NEi-NASTRAN with three different sets of boundary conditions (Corbishdale, 2014). One is done with no boundary conditions. The others are done with 1 Hz and 2 Hz vertical spring constraints. The spring constraints allow calculation of the percent modal mass of each elastic mode. The modal analysis was then repeated with ND NASTRAN for validation. The averaged differences between the reported results and those obtained from ND NASTRAN are 1.16%, 1.20% and 1.14% for all 200 modes respectively with free-free, 1 Hz and 2 Hz spring boundary conditions. The highest error is 2.97% in Mode 22 with free-free boundary condition. Three example results of modal analysis with all three boundary conditions are reported in Table 1 for both the reported and the newly obtained ones. The primary hull bending mode is a global mode of interest and the seat pedestal box mode and the aft cabin panel modes are the local modes associated with the pilot cabin. The percent modal masses of the global mode, the seat pedestal box mode and the aft cabin panel mode are about 70%, 0.2% and 3.3%, respectively.

2.3. Vertical acceleration data

Sea trials were conducted on an 11-meter RIB to investigate wave impact phenomena (Murphy and Planchak, 2015). The sea trials covered a wide range of speeds and significant wave heights. A total of 23 accelerometers were mounted around the boat to collect the acceleration data, mainly associated with vertical motion. The accelerometers were placed at the locations which are rigid and stiff to avoid the effects of

Table 1
ND NASTRAN model analysis sample results.

Modes	Free, Unconstrained		1 Hz Vertical Spring		2 Hz Vertical Spring	
	Initial Model	Current Study	Initial Model	Current Study	Initial Model	Current Study
Primary Hull Bending Mode	8.9 Hz	8.81 Hz	10.0 Hz	9.94 Hz	10.1 Hz	10.1 Hz
Seat Pedestal Box Mode	8.2 Hz	8.14 Hz	8.2 Hz	8.13 Hz	8.2 Hz	8.13 Hz
Aft Cabin Panel Mode	12.6 Hz	12.66 Hz	12.6 Hz	12.64 Hz	12.6 Hz	12.65 Hz

Table 2
Three envelopes of three seakeeping head sea runs.

	Testing Date	Target Seakeeping Runs; Head Sea	Average Craft Speed (Kn.)	Significant Wave Height (m)	Average Wave Period (Secs.)
Constant Speed Envelope	2/10/2014	Subcase 1	20.2	1.40	5.2
	3/11/2014	Subcase 2	20.5	0.67	7.2
	3/12/2014	Subcase 3	20.3	1.04	6.4
Constant Wave Height Envelope	2/12/2014	Subcase 1	25.7	1.19	5.6
	2/12/2014	Subcase 2	18.9	1.19	5.6
	2/21/2014	Subcase 3	14.9	1.19	5.7
Maximum Safe Speed Envelope	2/13/2014	Subcase 1	19.0	1.52	6.2
	3/11/2014	Subcase 2	35.8	0.70	7.5
	3/12/2014	Subcase 3	30.4	1.04	6.4

flexible vibration. Although the finite element model was highly detailed, it did not model all structural components with the same materials and properties as those in the physical RIB. As such, only fourteen accelerometers are used in this study, whose physical locations can be identified and associated with finite element nodal numbers. Eleven of them, 1Z, 2Z, 3Z, 4Z, 6Z, 7Z, 8Z, 9Z, 11Z, 17Z, and 21Z are selected for input of enforced excitation, while three of the fourteen, 10Z, 13Z and 16Z are for validation. The locations of all said accelerometers are presented in Figs. 1 and 2. The vertical accelerometers are marked with red arrows in Fig. 1, while they are marked with red dots in Fig. 2.

The accelerometers, 1Z, 3Z and 6Z are all aligned with the centerline around the keel and 2Z is also centered but placed in front of the engine box. The accelerometers 4Z and 7Z are placed on the deck plate, one is at transom and the other is in front of the pilot cabin. The rest of the accelerometers are placed around the cabin. The accelerometers 8Z and 9Z are placed respectively at the centerline and on the port side underneath the front bulkhead of the cabin. The accelerometer 10Z is centered on the deck plate inside the cabin, and the accelerometer 11Z is underneath the cabin door, near the LCG. The accelerometer 16Z is on the cabin top, while the accelerometers 13Z, 17Z and 21Z are all placed inside the cabin to measure the motions of the console and the seats on the port and starboard sides respectively.

Two types of accelerometers were used: Silicon Designs' Model 2260-025 and 2260-050. The sample rate of these accelerometers is set as 2000 per second in this study. These accelerometers could measure acceleration along three coordinate axes, and the positive coordinate directions are labeled on the accelerometer housings. The accelerometers were mounted so that the positive z-coordinate direction was pointed normal to the deck of the RIB and skyward. Efforts were made to keep the boat as level as possible during the sea trials; However, in rougher seas, it was much more difficult. It is assumed in this study that the planing craft during the sea trials was not subjected to large angular rotation. Consequently, the z-direction of the accelerometers remains parallel during the simulation to the z-direction of the global coordinate system which was the base in deriving the equation of motion, Eq. (7).

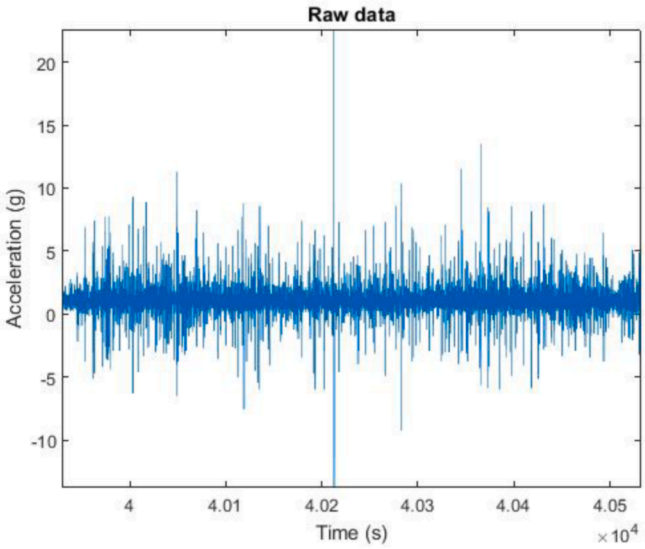

Fig. 3. Raw data of accelerometer 11Z.

Nine head-sea run data are selected in this study. Their information is summarized in Table 2. The data collected was categorized into three envelopes depending upon the conditions of head-sea runs. The top three runs listed in Table 2 make up the Constant Speed Envelope, where the average craft speed was approximately the same over three different wave-heights. The middle three runs make up the Constant Wave Height Envelope, where the significant wave-heights were about the same over three different average craft speeds. And the last three runs are where the RIB was at or near the maximum safe speed for the boat operator in the given ocean conditions and make up the Maximum Safe Speed Envelope. The maximum safe speed referred here was related to significant wave height. After approximately 1 m in significant wave height, the maximum speed of the boat had to be reduced in order to prevent risk of damage to the sensors and related equipment, the boat, and personnel. In-depth details of the data collection effort are presented in Murphy and Planchak (2015).

The acceleration data collected from sea trials are the results of the combined rigid body motion and the flexible vibration. To correlate the acceleration data with the impact force for a slamming event, a standardized process (Riley et al., 2010, 2012), has been developed in order to extract the rigid body dominated acceleration data associated with an isolated slamming event. The process first filters out the high frequency vibration modes and then sets up the amplitude and the time thresholds in order to identify the peaks of accelerations. Statistical terms of the collected peak acceleration data, such as RMS and the average of the highest one-third or one-tenth, can then be quantified to estimate the static-equivalent impact load. A *matlab* code, called the Standard G (Riley and Coats, 2013; Murphy and Planchak, 2015), developed based

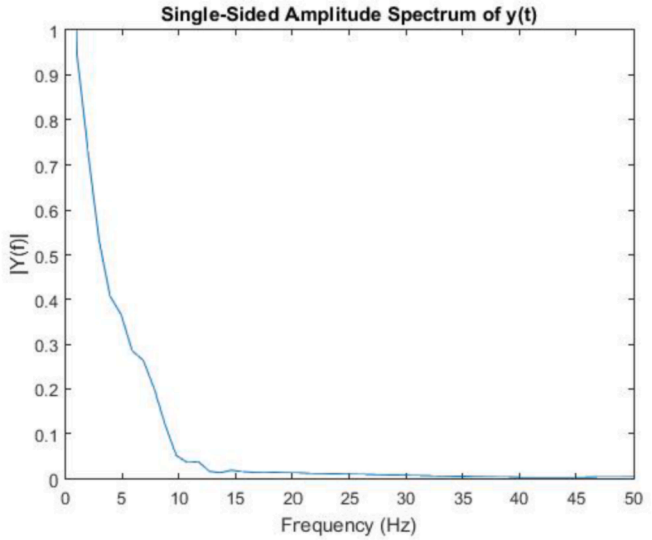

Fig. 4. Subcase 3 of constant speed envelope, 11Z full boat spectrum.

upon the described process, was used in this study to filter out the acceleration data around a peak of acceleration.

3. Full Boat Validation

The process begins with analysis of data collected during sea trials. The raw data collected from the accelerometer, 1Z, and the associated single-sided amplitude spectrum are displayed in Figs. 3 and 4 as an example input and output of the Standard G code. Fig. 4 demonstrates that the dominated modes are below 10 Hz, as suggested by Riley and Coats (2012a,b). The low-pass fourth-order Butterworth filter is then applied to the data set to remove the high frequency noise. The filtered data forms the base for the peak acceleration and wave impact counts.

In order to obtain meaningful results with manageable simulation time and data storage space, only one impact event is considered in this study for one specific sea trial run. The specific impact event is selected based upon the data collected from 11Z, which is located near the LCG. The highest peak of the acceleration is first identified. A total of 2000 data points before and after the highest peak to cover a period of one second are then collected to form the data set of a single wave impact. The data sets are all collected for the rest of 13 accelerometers with the same time frame as that of 11Z. This process is carried out for all

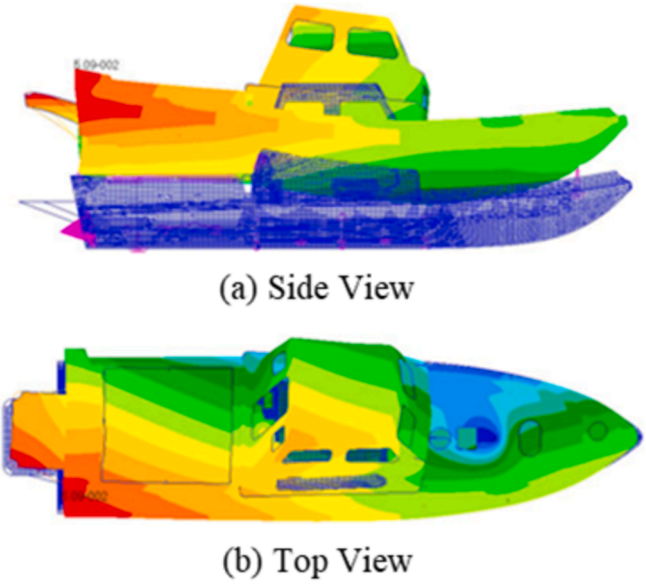

Fig. 6. Instantaneous deformation of the entire boat at 0.31 seconds during wave impact.

seakeeping runs listed in Table 2.

The full boat dynamic analysis is conducted by ND NASTRAN. The detailed input commands and examples for enforced transient analysis can be found in ND NASTRAN User Manual (2010). The procedure is mainly centered on two key bulk data commands, TLOAD1 and LSEQ. TLOAD1 provides the time history of the excited force, while LSEQ specifies the location where the excited force is imposed (Pamidi and Reymond, 2000). The TYPE entry in TLOAD1 is specified as ACCE so that the input data listed in Table 1 is taken as an enforced acceleration. The EXCITED entry in TLOAD1 is linked to the DAREA entry in LSEQ. LSEQ on the other hand refers to the SPCD command card to identify the nodal number where the excitation enforcement is imposed. The same nodal number is also referred in the SPC1 command card so that the node of concern and the associated degrees of freedom at which the acceleration is enforced can be treated as a single point boundary condition.

The entire simulation is done with a Dell desktop, model OPTIPLEX 990. Due to the limit on memory, only every fourth of the collected data are collected and included as input in the Table 1 format. This process is

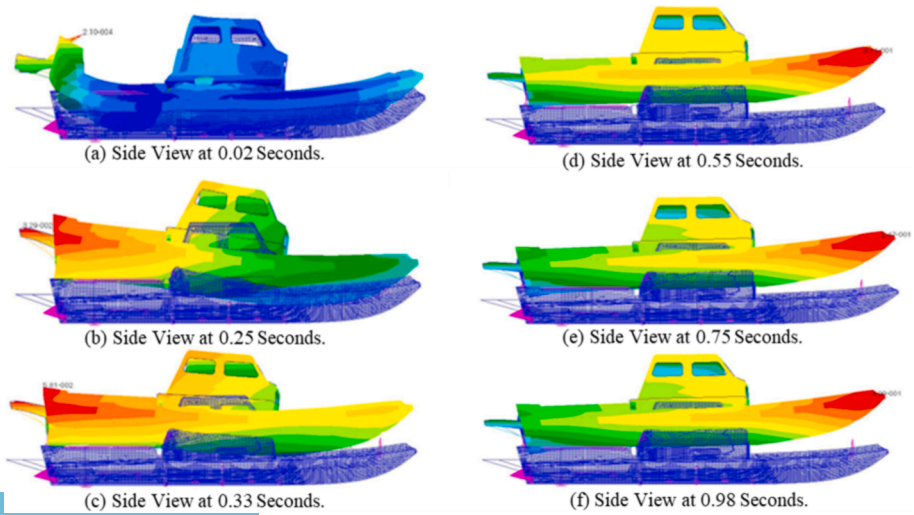

Fig. 5. Snapshots of boat movement in one second.

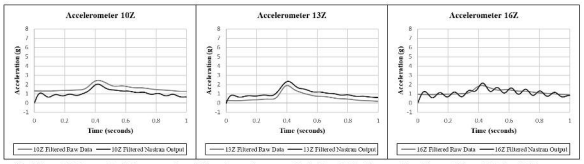

(b) Filtered Subcase 2 of Constant Speed Envelope. Average Craft Speed 20.5 knots. Significant Wave Height 0.67 meters. Average Wave Period 7.2 seconds.

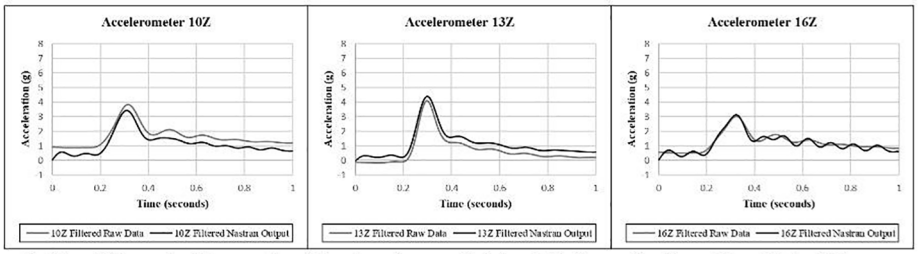

(c) Filtered Subcase 3 of Constant Speed Envelope. Average Craft Speed 20.3 knots. Significant Wave Height 1.04 meters. Average Wave Period 6.4 seconds.

Fig. 7. Filtered data comparisons for constant speed envelope.

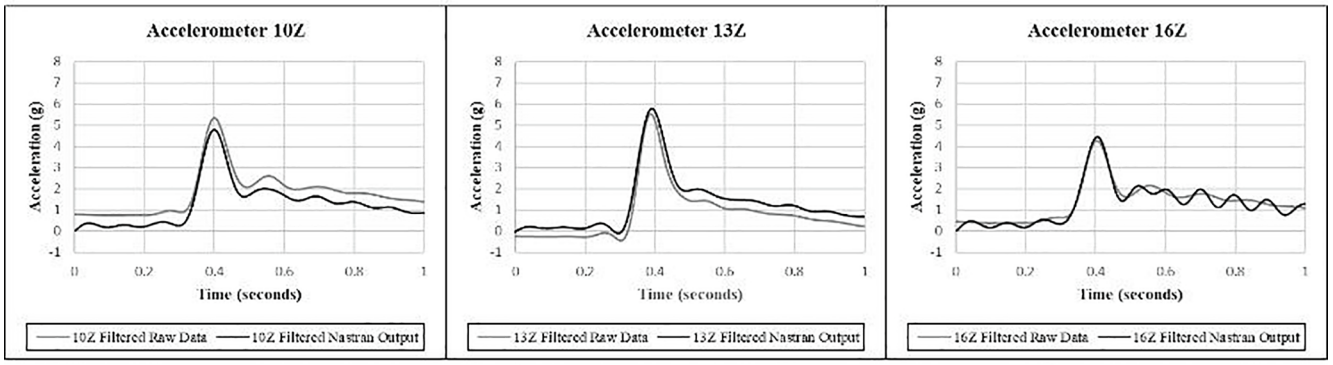

(b) Filtered Subcase 2 of Constant Wave Height Envelope. Average Craft Speed 18.9 knots. Significant Wave Height 1.19 meters. Average Wave Period 5.6 seconds.

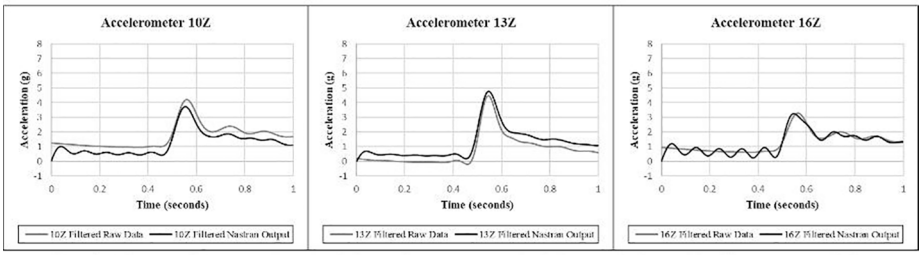

(c) Filtered Subcase 3 of Constant Wave Height Envelope. Average Craft Speed 14.9 knots. Significant Wave Height 1.19 meters. Average Wave Period 5.7 seconds.

Fig. 8. Filtered data comparisons for constant wave height envelope.

carried out for all 11 input acceleration data sets, associated with 1Z, 2Z, 3Z, 4Z, 6Z, 7Z, 8Z, 9Z, 11Z, 17Z, and 21Z. Limited by the simulation time and the computer memory, only two sets of output at the selected nodes are reported in these simulation runs; the nodal displacement and the nodal acceleration.

The sample snapshots of the motion profile of the boat during one second of a wave impact period are presented in Fig. 5 for the Subcase 3 seakeeping run in the constant speed envelope. The colors in the figures range from red to blue denoting the magnitudes of the point displacements from high to low. The dark blue mesh indicates the initial position of the vessel which starts with zero displacement and zero velocity. Particularly, Fig. 6 shows two different views of the instantaneous deformation of the entire boat at time 0.31 s which is at the acceleration peak during the constant speed, Subcase 3 seakeeping run. It can be observed that the boat heaves and pitches during this wave impact event.

The NASTRAN acceleration data at 10Z, 13Z and 16Z are output specifically for comparison purpose with the filtered raw data. Figs. 7–9 display the NASTRAN output data filtered at 10 Hz alongside with the full boat raw data, filtered also at 10 Hz for all three seakeeping envelopes, each of which has three subcases. The speeds of the vessels and wave conditions of these envelopes and subcases can be found in Table 2.

The simulation results match well with the raw data in the high and smooth acceleration regions. Also note that the simulation generates high frequency oscillation after the impact, which is not found in the

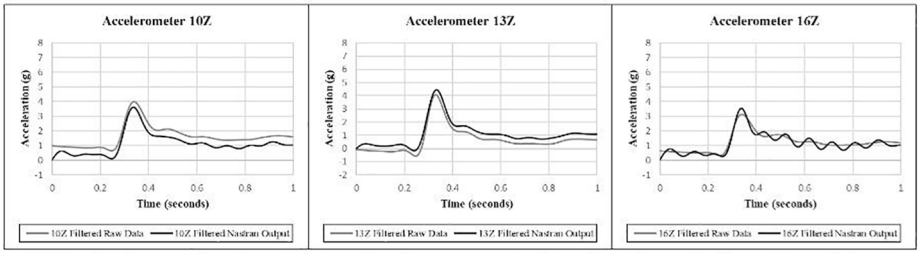

(b) Filtered Subcase 2 of Maximum Safe Speed Envelope. Average Craft Speed 35.8 knots. Significant Wave Height 0.70 meters. Average Wave Period 7.5 seconds.

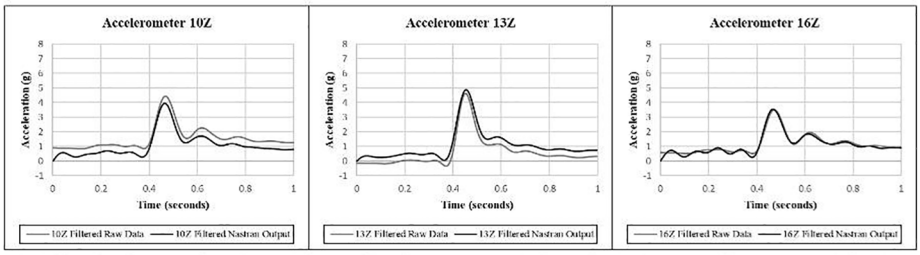

(c) Filtered Subcase 3 of Maximum Safe Speed Envelope. Average Craft Speed 30.4 knots. Significant Wave Height 1.04 meters. Average Wave Period 6.4 seconds.

Fig. 9. Filtered data comparisons for maximum safe speed envelope.

Table 3
Normalized Root Mean Square Deviation in g's: 11 Accelerometers as Input.

	Subcase	10Z Accelerometers, g's			13Z Accelerometers, g's			16Z Accelerometers, g's		
		RMSD		%	RMSD		%	RMSD		%
Constant Speed Envelope	1	0.551	6.48,0.29	8.90%	0.459	6.66, −0.89	6.10%	0.261	5.76, −0.89	3.90%
	2	0.497	2.46,1.26	41%	0.442	1.89, 0.20	26%	0.224	1.90, 0.92	22%
	3	0.486	3.85,0.87	16%	0.443	4.09, −0.18	10%	0.173	3.03,0.51	6.90%
	Pilot Cabin	0.4	3.85,0.87	13%	0.472	4.09, −0.18	11%	0.232	3.03,0.51	9.20%
Constant Wave Height Envelope	1	0.52	7.39,0.24	7.30%	0.476	7.62, −0.91	5.60%	0.224	6.48, −0.13	3.40%
	2	0.522	5.33,0.76	11%	0.471	5.54, −0.44	7.90%	0.205	4.27,0.38	5.30%
	3	0.495	4.20,0.97	15%	0.461	4.49, −0.19	9.80%	0.214	3.29,0.61	7.90%
Maximum Safe Speed Envelope	1	0.515	6.71,0.75	8.60%	0.487	7.53: −0.64	5.90%	0.177	5.41, 0.35	3.50%
	2	0.496	3.98,0.65	15%	0.443	4.07, −0.58	9.50%	0.211	3.15, 0.33	7.50%
	3	0.486	4.45, 0.86	14%	0.448	4.64, −0.33	9.00%	0.126	3.51, 0.51	4.20%

filtered raw data. This is particularly evident at the accelerometer 16Z which is mounted on the top of the pilot cabin, far away from the keel of the boat. To better quantify the difference between the raw data and the simulation output, the root-mean-square deviation, RMSD, and the normalized RMSD are calculated for each of the subcases. The results are tabulated in Table 3. Let the error, ε_i at the ith time instance, be defined as the difference between the filtered sea trial acceleration data, a_i^{exp}, and the filtered NASTRAN output, a_i^{sim}. That is,

$$\varepsilon_i = a_i^{exp} - a_i^{sim} \tag{9}$$

Based on Eq. (9), the RMSD is obtained for n total number of samples.

$$RMSD = \sqrt{\frac{\sum_{i=1}^{n} \varepsilon_i^2}{n}}$$

while the normalized RMSD represents the percentage deviation, relative to the range of the given data set

$$Normalized\ \ RMSD(\%) = \frac{RMSD}{\left(a_{i,max}^{exp} - a_{i,min}^{exp}\right)}$$

Data in Table 3 reveal that Subcase 2 of the Constant Speed Envelope has the highest percentage error among all subcases, while Subcase 2 of the Constant Wave Height Envelope has the lowest percentage error. The maximal acceleration of the former is lower than 2.46 g, while that of the latter is greater than 6.48 g. This observation implies that the acceleration-enforced dynamic simulation achieves better accuracy with higher peak acceleration impact. It is also interesting to notice that among all output accelerometers, 10Z, 13Z and 16Z, the simulation data at 16Z produces the most accurate results. The latter observation could be the result of the fact that 16Z is mounted at the top of the pilot cabin, farthest away from the keel of the boat. The elasticity of the vessel structure softens the impact of rigid modes on acceleration while promoting local, low amplitude vibration after impact. In fact, Fig. 7 through 9 appear to support this conclusion based on the higher acceleration frequency of 16Z in the unfiltered data as compared to the acceleration frequency of 10Z and 13Z.

4. Placement of accelerometers

In the enforced excitation, the input pointwise accelerations are viewed as the impact forces. Most of the 11 accelerometers selected as input for dynamic modeling are placed along the centerline and in the lower deck near the keel, except 3 accelerometers, 9Z, 17Z and 21Z. As shown in Fig. 2, all these three are placed at the base of the pilot cabin. The accelerometers, 17Z and 21Z, are symmetrically placed along the centerline; 17Z is on the port side, while 21Z is on the starboard. The accelerometer 9Z is placed on the port side, underneath the front bulkhead of the pilot cabin. The locations of these three accelerometers are far from the wet surface. Therefore, their accelerometers may not directly relate to the wave impact forces, rather they serve as the

Table 4
Percentage differences in normalized RMSD for different sets of input accelerometers.

Constant Speed Envelope: Subcase 3	10Z Accelerometer			13Z Accelerometer			16Z Accelerometer		
	RMSD	%	Diff in %	RMSD	%		RMSD	%	Diff in %
11 Accelerometers Input	0.4863	16.30%	–	0.4428	10.30%	–	0.1725	6.85%	–
9Z, 17Z, 21Z Removed	0.5206	17.40%	7.04	0.7231	16.90%	63.3	0.3324	13.20%	92.7
9Z, 17Z Removed	0.4396	14.70%	−9.6	0.5111	11.90%	15.4	0.3072	12.20%	78.1
9Z, 21Z Removed	0.4867	16.30%	1.57	0.4473	10.50%	12.8	0.2992	13.10%	90.6
17Z, 21Z Removed	0.494	16.50%	0.08	0.4996	9.83%	1.06	0.3287	11.90%	73.5
9Z Removed	0.4946	16.50%	1.7	0.4196	9.92%	−5.24	0.1755	6.97%	1.76
4Z, 9Z Removed	0.4929	16.50%	1.35	0.4232	9.45%	−4.42	0.1878	7.46%	8.9
8Z, 9Z Removed	0.5004	16.70%	2.89	0.4032	10.40%	−8.94	0.1768	7.02%	2.52

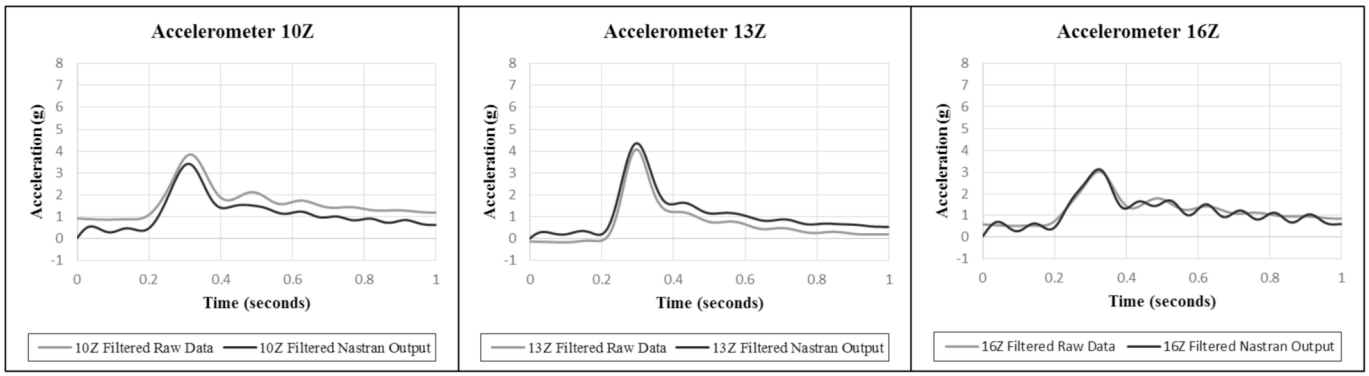

Fig. 10. Filtered data comparisons after accelerometers 8Z and 9Z removed.

enforced adjustment. This section first investigates the effects of these three off-center acceleration enforcements on the accuracy of the output pointwise accelerations at 10Z, 13Z and 16Z. It is then extended to include 4Z and 8Z in this study that are the accelerometers placed near the top deck. Note that the output accelerometers 10Z, 13Z, and 16Z, that are used for validation, are placed along the centerline of the pilot cabin; 10Z is on the base, 13Z the front midsection and 16Z the top of the pilot cabin.

The enforced dynamic simulations conducted in Section 3 are repeated here with different sets of input enforced accelerations that selectively excluded those accelerometers placed off-line or above deck height. Only Subcase 3 of the Constant Speed Envelope is selected as a demonstrative seakeeping run in this study. The vessel in this case runs with an average speed of 20.3 knots and an average wave period 6.4 seconds. The RMSD's and the associated normalized values of various scenarios with different sets of input accelerometers are summarized in Table 4, along with the data of the original runs for comparison.

It is observed that removal of accelerometers, involved 17Z and 21Z, which are on the port side and the starboard respectively will reduce the accuracy of the dynamic responses at three selected output accelerometers, which are mounted on the base, the front and the top of the pilot cabin. Particularly, large errors are observed at the output accelerometers, 13Z and 16Z which are on the front console and on the top of the pilot cabin. Removal of the un-symmetric accelerometer, 9Z, alone doesn't affect the accuracy of the output accelerometers, nor does removal of accelerometers 4Z and 8Z. Accelerometer 4Z locates at the stern on the top surface, right above 3Z which is mounted on the keel. Accelerometer 8Z is mounted on the base of the front bulkhead of the pilot cabin along the centerline. As an example, the acceleration output of the case with removal of 8Z and 9Z is plotted in Fig. 10 along with the sea trial raw data. Note that Fig. 7(c) displays the initial acceleration responses without removing 8Z and 9Z from input data set.

In a summary, two primary conclusions may be drawn from the study in this section. One, it is more important to place the enforced accelerometers along the keel or near to it than those high above it. And two, it is beneficial to place the input enforced accelerometers around the structural area of concern, particularly if this area is flexible. In this case, these enforced accelerometers serve as constraints or adjustments, rather than the representations of the input excitation forces.

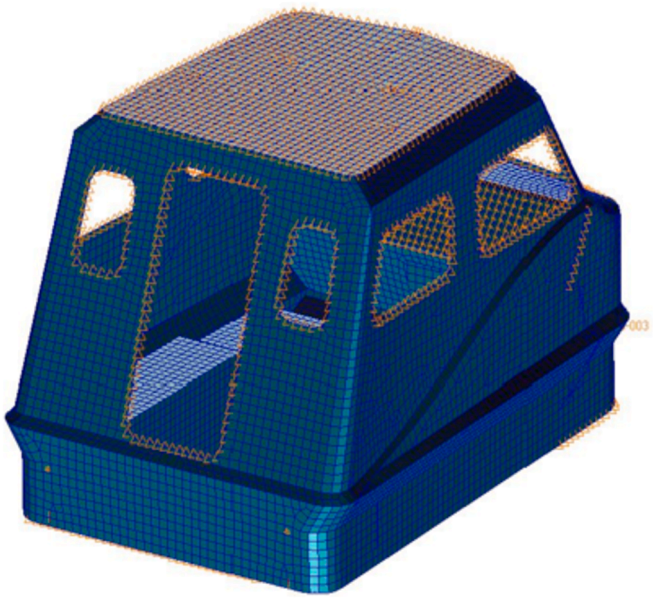

Fig. 11. Isolated pilot cabin.

5. Dynamic substructure analysis of the pilot cabin

Dynamic substructure analysis could be used to accomplish refined analysis without imposing a burden on computer resources. In this study, one will focus on the vibration characteristics of the pilot cabin, which affects onboard instrument noise and crew comfortability while

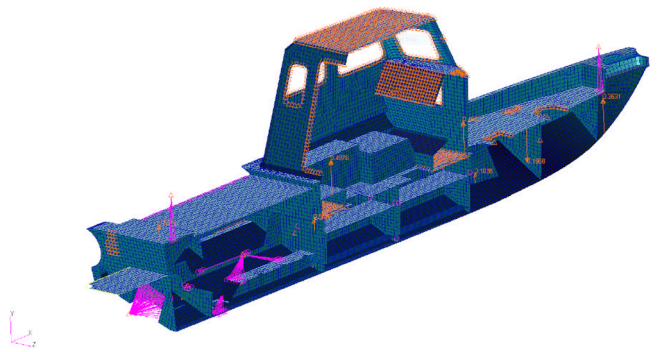

Fig. 12. Side-view of cabin and transverse bulkheads of 11 meter RIB model.

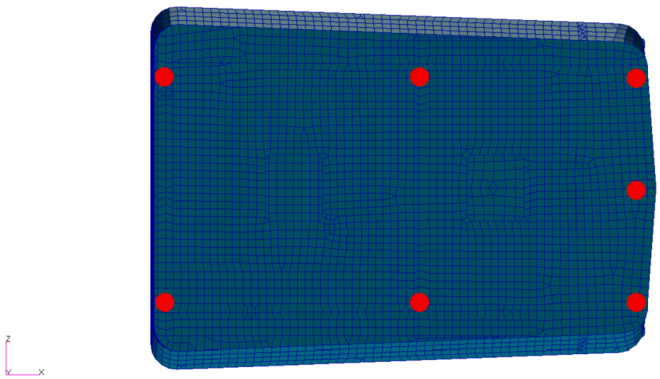

Fig. 13. Locations of seven input acceleration nodes on the base of pilot cabin.

operating a RIB. The finite element model of the pilot cabin isolated from the main deck of the RIB is shown in Fig. 11. The base of the pilot cabin is rectangular around 1.92 by 2.92 m (75.5 by 115 inches). The dynamic analysis of the pilot cabin during a wave impact is carried out following the same acceleration enforcement procedure as presented before. However, in this case, the input accelerations at the selected points on the base of the isolated pilot cabin are taken not from the sea trials but from the full boat dynamic analysis conducted in Section 2. To this end, it is necessary to select an appropriate set of input base excitation accelerations as well as their locations.

Ideal locations for the input acceleration nodes are assumed to be at the top of bulkheads, beneath the cabin, for the rigidity of the bulkheads. However, in the current design, the walls of the pilot cabin at its base are not aligned with the bulkhead intersections. Therefore, the nodes on the base of the cabin that are closest to the intersections of the transverse and the longitudinal bulkheads are first selected as the cabin input acceleration. Three additional acceleration input nodes are then selected; one is on the middle section along the port side of the pilot cabin, another along the starboard and the other is at the center of the front bulkhead. At the end, seven acceleration input nodes in total are selected in this study. The side view of the transverse bulkhead and the pilot cabin is shown in Fig. 12, while the locations of the seven input acceleration nodes are marked in Fig. 13 on the mesh model of the base of the pilot cabin. Note that like those in Figs. 1 and 2, the purple bars in Figs. 11 and 12 mark the rigid bar elements connecting lumped masses to the key structural nodes and the orange nodes are those with smeared masses.

Next, the acceleration data at the seven selected nodes are taken from the output of the full boat dynamic analysis, filtered out at 10 Hz, and then input as the enforced base excitation for the dynamic analysis of the isolated pilot cabin model. This is carried out only for Subcase 3

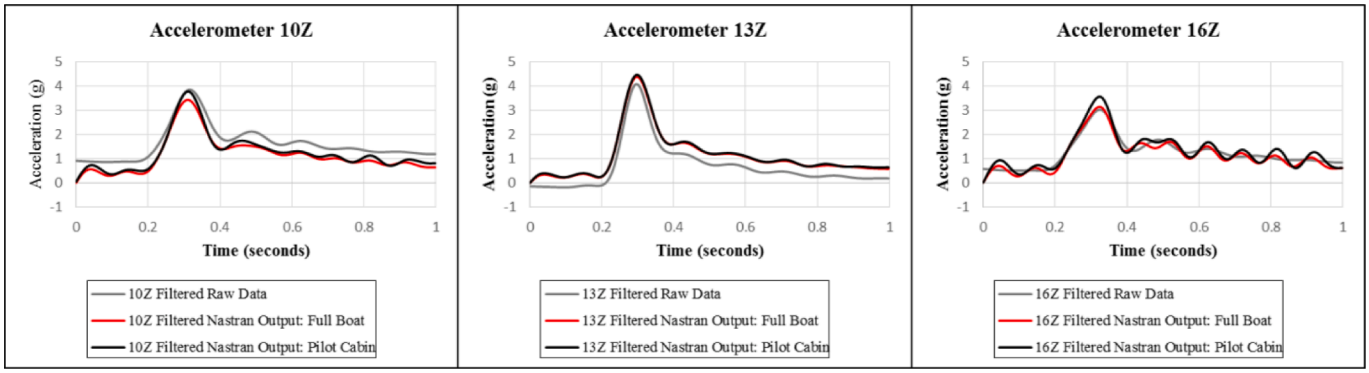

(a) Data Filtered at 10 Hz

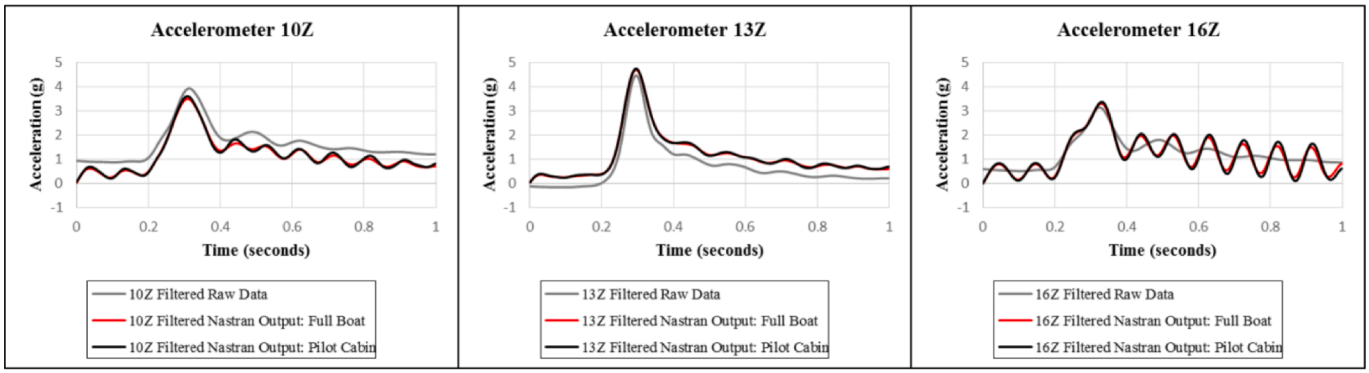

(b) Data Filtered at 13 Hz

Fig. 14. Isolated pilot cabin analysis validation.

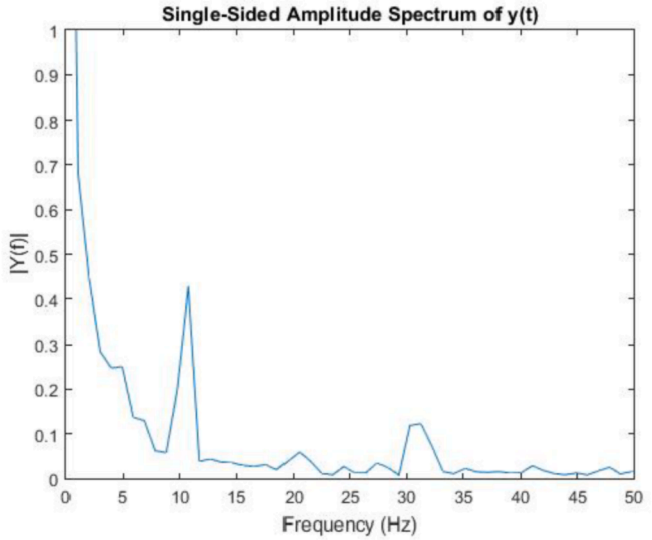

Fig. 15. 16Z accelerometer spectrum plot for subcase 3 of constant speed envelope.

seakeeping trial run of the constant speed envelope. The output of acceleration data at 10Z, 13Z and 16Z mounted on the pilot cabin are selected and compared with the sea trial acceleration data as well as those out of the full boat dynamic analysis. All these data are filtered out at 10 Hz and displayed in Fig. 14(a). It is evident that all three cases engage high local vibration after peak acceleration. This is particularly significant in accelerometer 16Z which is on the top of the pilot cabin. This leads to the reinvestigation of the spectrum plot of the raw acceleration data at 16Z. Fig. 15 shows that the frequencies ranging between 9 and 12 Hz do contribute significantly to the content of 16Z acceleration. In fact, Corbishdale (2014) reported in his full boat finite element modal analysis that significant local modes related to the pilot cabin are at 11.2 Hz and 12.6 Hz. Consequently, the dynamic substructure analysis is repeated by filtering out the output of the full boat dynamic analysis at 13 Hz before taking them as input to enforce excitation. The newly obtained results are plotted in Fig. 14(b). When filtered at a higher frequency, more local vibration modes are observed due to the high frequency filtered enforced excitation. Results show that a 45% reduction in normalized RMSD from 0.0558 to 0.0306 is observed when filtered at 13 Hz instead of 10 Hz. This example demonstrates that the dynamic analysis of a full boat with enforced acceleration can be successfully extended to an isolated substructure, if the number and the location of the interface excitation nodes are properly selected. This is done without any additional sea trial data.

As a final investigation, the acceleration and the stress output around the seat pedestals are collected for the isolated pilot cabin. All these results reported here are filtered at 13 Hz. The acceleration plots for the port seat pedestal and the starboard seat pedestal are summarized in Fig. 16 for a single wave impact. It is interesting to notice that, after peak impact, both seat pedestals are subjected to around 8 Hz of high acceleration repeated impact, which are not noticeable in the output of all other accelerometers in this study. This conclusion, however, is drawn only for Subcase 3 sea trial of Constant Speed Envelope.

Due to the requirement of a large data storage space, NASTRAN is unable to report the stress time history for the full RIB model. As the size of the finite element model is reduced, it is then feasible to report the stress contour time history of the entire isolated pilot cabin. Particularly, the von Mises stress histories during a wave impact at the port and the

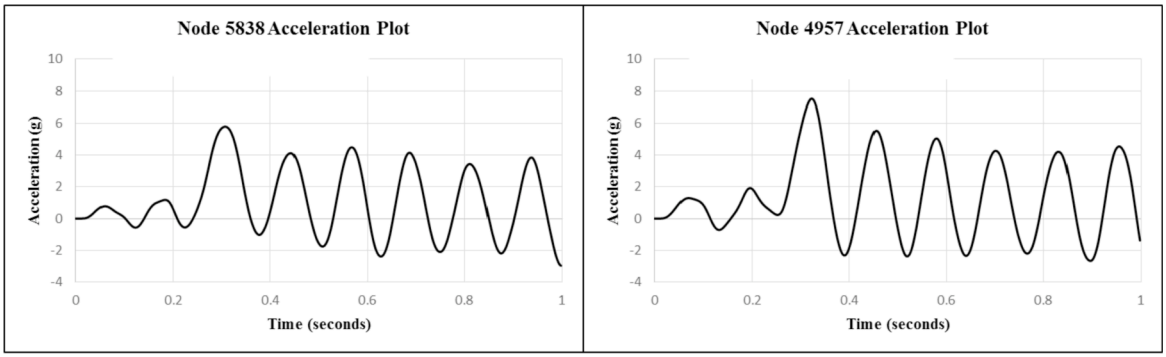

Fig. 16. The acceleration profiles of the port seat pedestal and the starboard seat pedestal.

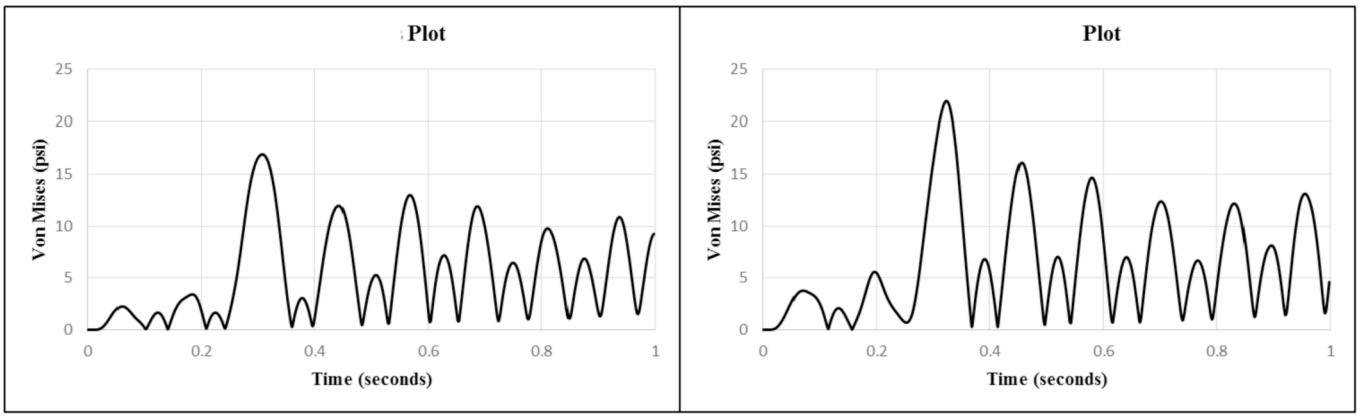

Fig. 17. The von Mises Stress Histories of the Port Seat Pedestal and the Starboard Seat Pedestal
(a) Von Mises Stress Contour Plot at 0.298 Seconds. (b) Von Mises Stress Contour Plot at 0.458 Seconds.

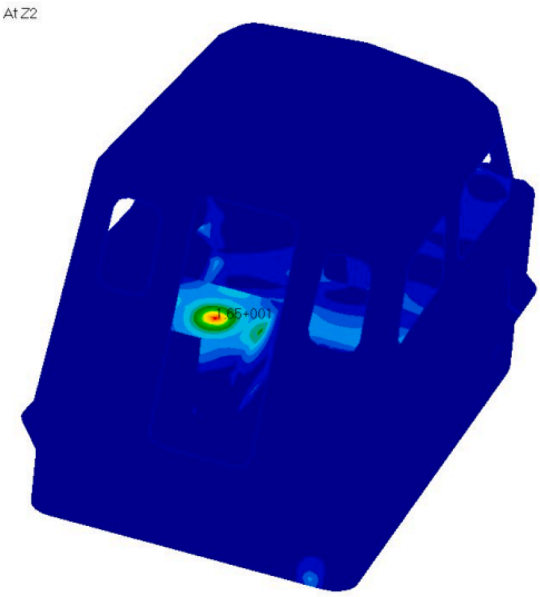

(a) Von Mises Stress Contour Plot at 0.298 Seconds

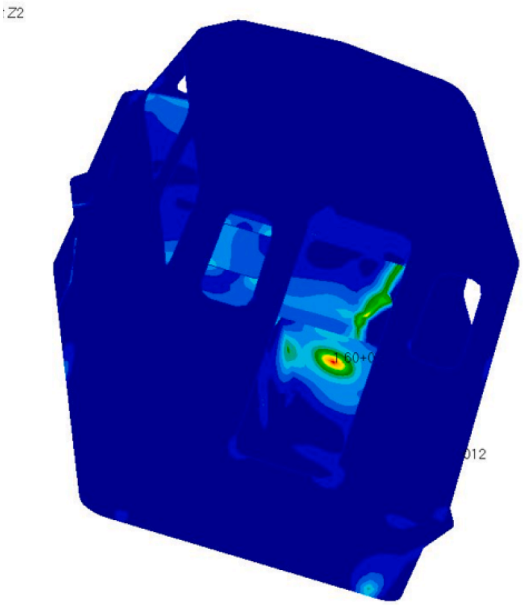

(b) Von Mises Stress Contour Plot at 0.458 Seconds

Fig. 18. Stress contour plots at two acceleration peaks.

starboard seat pedestals are selected and plotted in Fig. 17. And the stress contour plots of the pilot cabin are reported at time 0.298 s and 0.458 s, respectively in Fig. 18. The first plot in Fig. 18(a) is associated with the first acceleration peak of the port seat pedestal at 0.298 s, while the second plot in Fig. 18(b) is with the second acceleration peak of the starboard seat pedestal at 0.458 s.

6. Conclusion and recommendations

The development of methods and procedures to better understand the dynamic responses of high-speed planing hulls to wave impacts is necessary in order to mitigate risk to crew and equipment. In the current work, the structure dynamic analysis of a high-speed planing craft is completed by enforcing the collected pointwise acceleration data on a valid finite element model. The thoughtfully built finite element model of a RIB, along with the acceleration data collected from sea trails, are essential to facilitate this study.

The proposed method is validated by focusing on nine single wave impacts, each of which is associated with one specific seakeeping condition selected from the available sea trial data. The acceleration data acquired from 11 accelerometers placed inside the lower boat hull are selected as the input enforced acceleration, while those collected from 3 accelerometers mounted on the top and the base of the pilot cabin are used to investigate the accuracy of the simulation. The results demonstrate that the output of the proposed method matches well with those of sea trial data. Particularly, the proposed method achieves higher accuracy for the higher peak acceleration case than for the lower ones. For example, the simulation achieves less than 7.3% error measured by the normalized RMSD, for the seakeeping run with an average craft speed of 18.9 knots, significant wave height 1.19 m and wave period of 5.6 s. The peak acceleration in this case collected during sea trials ranges from 6.48 g to 7.39 g in the three output accelerometers mounted around the pilot cabin. The high peak acceleration is usually a condition of major concern for design and operation of a high-speed planing hull.

In the second phase of this study, the issue about the number and the placement of input accelerometers is investigated. The accelerometers aligned along the keel and near the bottom hull are found to be more important to the accuracy of the simulation than those away and off the centerline. Furthermore, it is beneficial to place the input accelerometers around the base of the pilot cabin. Even though these accelerometers do not directly represent the impact load, they are the constrained forces which adjust the solution of the substructure that is placed far away from the keel.

Finally, the enforced acceleration method is extended successfully to conduct the dynamic analysis of an isolated pilot cabin. The input acceleration data set is selected from the output of the full boat numerical simulation to excite the pilot cabin. This approach allows for more focused, efficient and comprehensive substructure analysis which is needed for mounting instrument and crew seats onboard a high-speed craft.

This paper represents an initial attempt to employ the base excitation method for dynamic analysis of a high-speed craft with the enforced acceleration based upon the sea trial data. This method is structure-based, doesn't involve computational fluid dynamics nor fluid-structure interaction. Though the effects of structural damping and large pitching movement were not considered in this study, the results of this study were validated satisfactorily. It should be noticed that its success relies upon the accurate finite element model and the carefully filtered acceleration data.

The successful demonstration presented in this paper has opened a door for more broad investigation of the proposed method. One is to calculate the constraint loads, λ, in Eq. (8), which are the ones to enforce the prescribed motion. The magnitudes of λ, could be useful to correlate the pressure load distribution to acceleration and provide an insight into selecting proper locations to place accelerometers. The other is to extend the method to simulate a planing hull operated under large pitching and yawing conditions. In these cases, additional sensor data such as those collected from IMU, 3-axis accelerometers and strain gauges may be used for further enforcement and validation.

Acknowledgements

This research was partially funded by the Naval Engineering Education Consortium (NEEC), under the Navy Grant N0017416C0031 awarded to Old Dominion University Research Foundation. The authors would like to express their gratitude to Dr. Timothy Coats, Combatant Craft Division, Naval Surface Warfare Center Carderock Division (NSWCCD), for his invaluable assistance.

References

Allen, R.G., Jones, R.R., Taylor, D.W., 1978. A simplified method for determining structural design-limit pressures on high performance marine vehicles. In: Proceedings of the AIAA/SNAME Advanced Marine Vehicle Conference. San Diego, CA.

Aymone, J.L.F., 2004. Mesh motion techniques for the ALE formulation in 3D large deformation problems. Int. J. Numer. Methods Eng. 59, 1879–1908.

Bampton, M.C., Craig, R.R., 1968. Coupling of substructures for dynamic analyses. AIAA J. 6 (7), 1313–1319. https://doi.org/10.2514/3.4741.

Blades, E.L., Craig, R.R., 1997. A Craig-Bampton test-analysis model. In: Proc. SPIE-Int. Soc. Opt. Eng., pp. 1386–1391.

Carrica, P.M., Huang, J., Noack, R., Kaushik, D., Smith, B., Stern, F., 2010. Large-scale DES computations of the forward speed diffraction and pitch and heave problems for a surface combatant. Comput. Fluid 39, 1095–1111.

Chandrupatla, T.R., Belegundu, A.D., 2012. Introduction to Finite Elements in Engineering. Prentice Hall, Upper Saddle River, NJ.

Cho, D.S., Kim, B.H., Kim, J., Vladimir, N., Choi, T.M., 2016. Frequency response of rectangular plates with free-edge openings and carlings subjected to point excitation force and enforced displacement at boundaries. J. Nav. Archit. Ocean Eng. 8 (2), 117–126. https://doi.org/10.1016/j.ijnaoe.2015.06.001.

Clough, R.W., Penzien, J., 1975. Dynamics of Structures. McGraw-Hill, New York, NY.

Corbishdale, A.J., 2014. Finite Element Model Creation and Modal Analysis of a Zodiac H1110 AFT IO CABIN RIB for the Wave-Slam Phenomenology and Transmissibility of a High-Speed Planing Craft Core R&D Project. Naval Surface Warfare Center, Carderock Division.

Davis, M.D., Tedesco, S., Huynh, T., Hou, G., 2012. Finite element transient analysis of flexible structure under wave slamming environment. In: Proceedings of the 4th International Forum on Systems and Mechatronics, pp. 214–231. Virginia Beach, VA.

Dessi, D., Ciappi, E., 2013. Slamming clustering on fast ships: from impact dynamics to global response analysis. Ocean Eng. 62, 110–122.

Faltinsen, O.M., 2005. Hydrodynamics of High-Speed Marine Vehicles. Cambridge University Press, New York, NY.

Flanigan, C.C., 1994. Accurate enforced motion analysis using MSC/NASTRAN super-elements. In: 1994 MSC/NASTRAN World Users Conference. Orlando, FL.

Fragassa, C., 2019. Engineering design driven by models and measures: the case of a rigid inflatable boat. J. Mater. Sci. Eng. 7 (6).

Fragassa, C., Topalovic, M., Vulovic, S., Pavlovic, A., 2019. Dealing with the effect of air in fluid structure interaction by coupled SPH-fem methods. Materials 12 (1162), 1–17.

Fridsma, G., 1971. A Systematic Study of the Rough Water Performance of Planing Boats – Irregular Waves – Part II (Rep.). Stevens Institute of Technology, Hoboken, NJ.

Grimsley, J., Liu, Y., Hou, G., 2010. An examination of the statistical behavior of planing craft peak vertical accelerations in irregular waves. In: Proceedings of the 29th American Towing Tank Conference, pp. 31–39. Annapolis, MD.

H1110 Zodiac, 2005. Hurricane Technologies, Inc. https://zodiacmilpro.com/wp-content/uploads/2010/02/1110AFTIOCabin2.pdf.

Haug, E.J., 1989. Computer-Aided Kinematics and Dynamics of Mechanical Systems, vol. 1. Allyn and Bacon Series in Engineering. Basic Methods.

Haug, E.J., 1992. Intermediate Dynamics. Prentice-Hall, Inc.

Hoggard, M., Jones, M., 1980. Examining pitch, heave, and accelerations of planing craft operating in a seaway. In: High-Speed Surface Craft Exhibition and Conference. Metropole, Brighton, U.K.

Hou, G., Wang, J., Layton, A., 2012. Numerical methods for fluid-structure interaction – A review. Commun. Comput. Phys. 12 (2), 337–377.

Hu, D., Long, T., Xiao, Y., Han, X., Gu, Y., 2014. Fluid-structure interaction analysis by coupled FE-SPH model based on a novel searching algorithm. Comput. Methods Appl. Mech. Eng. 276, 266–286.

Joo, H.K., Mohamad, M.A., Sapsis, T.P., 2017. Extreme events and their optimal mitigation in nonlinear structural system excited by stochastic loads: application to ocean engineering systems. Ocean Eng. 142, 145–160.

Liu, M.B., Liu, G.R., 2010. Smoothed particle hydrodynamics (SPH): an overview and recent developments. Arch. Comput. Methods Eng. 17, 25–76.

Liu, Y., Lu, Z., 2010. Methods of enforcing earthquake base motions in seismic analysis of structures. Eng. Struct. 32 (8), 2019–2033. https://doi.org/10.1016/j.engstruct.2010.02.035.

Ma, S., Mahfuz, H., 2012. Finite element simulation of composite ship structures with fluid structure interaction. Ocean Eng. 52, 52–59.

MD-NASTRAN 2010 Dynamic Analysis User Guide, 2010. Chapter 7: Enforced Motion. MSC Software. http://www.scribd.com/doc/34668635/MD-Nastran-2010-Dynamic-Analysis-User-s-Guide#scribd.

Murphy, H.P., Planchak, C.J., 2015. Description of the Rough-Water Dataset Captured on a Shallow-Vee Hull. Naval Surface Warfare Center, Carderock Division., West Bethesda, MD. Technical Report, NSWCCE-80-TR-2015/XXX.

Nordanger, K., Rsheed, A., Okstad, A.R., Kvarving, A.M., Holdahl, R., Kvamsdal, T., 2016. Numerical benchmarking of fluid-structure interaction: an isogeometric finite element approach. Ocean Eng. 124, 324–339.

Ojeda, R., Prusty, G., Marcos, R.S., 2004. Finite element investigation on the static response of a composite catamaran under slamming loads. Ocean Eng. 31 (7), 901–929.

Pamidi, P.R., Reymond, M., 2000. Improvement to dynamic analysis in MSC.nastran, MSC software corporation. In: Presented at the 2nd MSC Worldwide Automotive Conference, Oct. 9-11, Dearborn, MI. http://web.mscsoftware.com/support/library/conf/auto00/p04200.pdf.

Razola, M., Rosen, A., Garme, K., 2014. Allen and Jones revisited. Ocean Eng. 89, 119–133.

Razola, M., Olausson, K., Garme, K., Rosen, A., 2016. On high-speed craft acceleration statistics. Ocean Eng. 114, 115–133.

Reddy, J.N., 1984. An Introduction to the Finite Element Method, second ed. McGraw Hill.

Riley, M.R., Coats, T.W., 2012. A method for computing wave-impact equivalent static accelerations for use in planing craft hull design. In: Presented in the Third Chesapeake Power Boat Symposium, Annapolis, MD, pp. 15–16. June 2012. http://www.tvworldwide.com/events/powerboatsymposium/120615/default.cfm?id=14780&type=flv&test=0&live=0.

Riley, M.R., Coats, T.W., 2012. A simplified approach for analyzing accelerations induced by wave-impacts in high-speed planing craft. In: Presented in the Third Chesapeake Power Boat Symposium, Annapolis, MD, pp. 15–16,. http://www.tvworldwide.com/events/powerboatsymposium/120615/default.cfm?id=14778&type=flv&test=0&live=0.

Riley, M.R., Coats, T.W., 2013. The Simulation of Wave Slam Impulses to Evaluate Shock Mitigation Seats for High-Speed Planing Craft. NSWCCD-83-TM-2013/26. Naval Surface Warfare Center, Carderock Division. https://apps.dtic.mil/dtic/tr/fulltext/u2/1042130.pdf.

Riley, M.R., Peterson, S.M., 2017. The Use of Shock Isolation Mounts in Small High-Speed Craft to Protect Equipment from Wave Slam Effects. NSWCCD-80-TR-2017/022. Naval Surface Warfare Center, Bethesda, MD. Carderock Division. https://apps.dtic.mil/dtic/tr/fulltext/u2/1037851.pdf.

Riley, M.R., Haupt, K., Jacobson, D., 2010. A Generalized Approach and Interim Criteria for Computing A1/n Accelerations Using Full-Scale High-Speed Craft Trials Data. NSWCCD-23- TM 2010/13. Naval Surface Warfare Center, Carderock Divsion. April 2010. https://apps.dtic.mil/dtic/tr/fulltext/u2/a640546.pdf.

Riley, M.R., Haupt, K.D., Jacobson, D.R., 2012. A Deterministic Approach for Characterizing Wave Impact Response Motions of a High-Speed Planing Hull. NSWCCD-23-TM 2012/05. Naval Surface Warfare Center, Carderock Divsion. https://apps.dtic.mil/dtic/tr/fulltext/u2/a639787.pdf.

Riley, M.R., Murphy, H.P., Coats, T.W., 2016. A Consistent Wave Impact Load Model for Studying Structure, Equipment Ruggedness, Shock Isolation Seats, and Human Comfort in Small High-Speed Craft. NSWCCD-80-TR-2016/033. Naval Surface Warfare Center, Bethesda, MD. Carderock Division. https://apps.dtic.mil/dtic/tr/fulltext/u2/1042127.pdf.

Rosen, A., 2005. Impact pressure distribution reconstruction from discrete point measurements. Int. Shipbuild. Prog. 52 (1), 91–107.

Rosen, A., Garme, K., 2004. Model experiment addressing the impact pressure distribution on planing craft in waves. Int. J .Small Craft Technol. 146.

Savitsky, D., Brown, P.W., 1976. Procedures for hydrodynamic evaluation of planing hulls in smooth and rough water. Mar. Technol. 13 (4), 381–400.

Scovazzi, G., Song, T., Zheng, X., 2017. A velocity/stress mixed stabilized nodal finite element for elastodynamics: analysis and computations with strongly and weakly enforced boundary conditions. Comput. Methods Appl. Mech. Eng. 325 (1), 532–576.

Siemann, M.H., Langrand, B., 2017. Coupled fluid-structure computational methods for aircraft ditching simulations: comparison of ALE-FE and SPH-fe approaches. Comput. Struct. 188, 95–108.

Sukas, O.F., Kinaci, O.K., Cakici, F., Gokce, M., 2017. Hydrodynamic assessment of planing hulls using overset grids. Appl. Ocean Res. 65, 35–46.

VanDerwerken, D., Judge, C., 2017. Statistical analysis of vertical accelerations of planing craft: common pitfalls and how to avoid them. Ocean Eng. 1 (39), 265–274.

Volpi, S., Diez, M., Sada-Hosseini, H., Stern, F., Thodal, R.S., Grenestedt, J.L., Kim, D.-., 2017. Composite bottom panel slamming of a fast planing hull via tightly coupled fluid-structure interaction simulations and sea trials. Ocean Eng. 143, 240–258.

Xie, H., Ren, H., Qu, S., Tang, H., 2018. Numerical and experimental study on hydroelasticity in water-entry problem of a composite ship-hull structure. Compos. Struct. 201, 942–957.

Yang, L., 2018. One-fluid formulation for fluid-structure interaction with free surface. Comput. Methods Appl. Mech. Eng. 332, 102–135.

Yang, C., Huang, F., 2016. An overview of simulation-based hydrodynamic design of ship hull forms. J. Hydrodyn. 6, 947–960.